EARTH SURFACE PROCESSES AND LANDFORMS
Earth Surf. Process. Landforms **38**, 275–283 (2013)

Published online 27 September 2012 in Wiley Online Library
(wileyonlinelibrary.com) DOI: 10.1002/esp.3323

Advances in automated detection of sand dunes on Mars

Lourenço Bandeira,[1]* Jorge S. Marques,[2] José Saraiva[1] and Pedro Pina[1]
[1] CERENA-Centro de Recursos Naturais e Ambiente, Instituto Superior Técnico, Lisboa, Portugal
[2] ISR – Instituto de Sistemas e Robótica, Instituto Superior Técnico, Lisboa, Portugal

Received 31 May 2011; Revised 29 August 2012; Accepted 30 August 2012

*Correspondence to: Lourenço Bandeira, CERENA-Centro de Recursos Naturais e Ambiente, Instituto Superior Técnico, Av. Rovisco Pais, 1049–001 Lisboa, Portugal.
E-mail: lpcbandeira@ist.utl.pt

ESPL
Earth Surface Processes and Landforms

ABSTRACT: This paper describes advances in an automatic approach for the detection of sand dunes of Mars, based on supervised learning techniques. A set of features (gradient histogram) is extracted from the remotely sensed images and two classifiers (Support Vector Machine and Random Forests) are trained from this data. The evaluation is conducted on 230 MOC-NA images (spatial resolution between 1·45 and 6·80 m/pixel) leading to about 89% of correct detections. A detailed analysis of the detection results (dune/non-dune) is performed by dune type or bulk shape, confirming high performances independently of the way the dataset is analysed. This demonstrates the robustness and adequacy of the automated approach to deal with the large variety of aeolian structures present on the surface of Mars. Copyright © 2012 John Wiley & Sons, Ltd.

KEYWORDS: pattern recognition; gradient histogram features; supervised learning; dunes; Mars

Introduction

In recent years, research into the use of automated methods for feature and change detection of structures on planetary surfaces has greatly increased, due to the need to process larger amounts of remotely sensed imagery with lower limits of spatial detection, where sub-metric patterns can be recognized without ambiguity, in objective and more precise modes. This is also valid for aeolian features, in particular for those of Mars, where the availability of such approaches could largely expand our knowledge about the characteristics of those features (Fenton and Hayward, 2010), currently mainly based on moderate to large dimension dunes (Hayward *et al.*, 2007, Bourke *et al.*, 2010). In particular, some semi-automated approaches have been developed to address temporal change detection (Silvestro *et al.*, 2010), to measure dune heights (Bourke *et al.*, 2006) and morphologies (Ewing *et al.*, 2006), to make three-dimensional (3D) spatial analysis (Hugenholtz and Barchyn, 2010), or to contribute to understand dune self-organization patterns (Bishop, 2010), on the surfaces of Earth and Mars. A search in the literature for automated dune detection revealed, other than our method (Bandeira *et al.*, 2010, 2011), only one other recent approach based on texture features and neural networks (Chowdhury *et al.*, 2011): here, terrestrial multispectral images were employed with a spatial resolution of 23·5 metres/pixel, to classify small blocks of 17×17 pixels using the grey level co-occurrence matrix, achieving a detection rate below 70%. In our method, based on image analysis and pattern recognition techniques, the aim was to detect sand dunes on remotely sensed images of the surface of Mars, using four sets of image features based on the combination of image gradient parameters that were tested to detect the presence (or absence) of dunes in the images, within blocks of given dimensions, with two distinct classifiers, SVM-Support Vector Machines and Boosting, obtaining overall performances as good as 95% of correct detections on 78 MOC-NA images covering a surface of about 5000 km^2. The main conclusion drawn from that work was that three out of the four sets of features performed extremely well with both classifiers, making almost indifferent the option between SVM and Boosting to carry out the classifications. These results permitted the approach presented to be validated and to be confident enough about the potentiality of its widespread application to images from anywhere on the Martian surface. Nevertheless, although a diversified image dataset was used containing examples from both hemispheres of Mars, images acquired along the full range of solar longitudes and with distinct solar illuminations, the dunes present were mainly of the barchan and barchanoid types. In this work we widened the scope of the image dataset to include all types of Martian dunes, both those similar to terrestrial types (McKee, 1979) and those only found on Mars (Hayward *et al.*, 2007), creating a new set of 160 images.

Thus, this paper presents advances in automatic dune detection, using a set of features computed from the histogram of gradient magnitude and phase in nine cells of 40×40 pixels. These features are detailed in Bandeira *et al.* (2011), under the acronym HPM9. Two state-of-the-art classifiers are considered in this work: SVM-Support Vector Machines (Vapnik, 1995) and RF-Random Forests (Breiman, 2001); the latter is new relative to earlier work (Bandeira *et al.*, 2011), and serves to verify if it can produce better results than SVM (which was not the case with Boosting). In the next section, we describe the automated approach supported by a sequence of illustrations. The datasets

and strategy used for the evaluation are presented in the third section. The results on the performances according to the type of dune and global bulk shape are presented and discussed in the fourth section. Finally, in the fifth section, the conclusions and the lines of research to be pursued in future work are presented.

Methodology for Automated Detection of Sand Dunes

In this section we describe briefly how our methodology works. For the mathematical formalism and additional details, we advise readers to consult the work where the method was presented in depth (Bandeira *et al.*, 2011).

The strategy followed in our approach is based on the classification of small square regions of the image (with 40×40 pixels), called cells (Figure 1a). The use of a simple geometric shape (such as a square) as a cell makes its analysis very fast and leads to a non-iterative solution which is compatible with the large amount of data to be processed.

This task is done through the extraction and analysis of local information (image features) along the regular grid of a tiled image. To benefit from the context and diminish the dependence on specific environmental factors such as illumination and shadowing, an aggregation of the local features of neighbouring cells is performed within a block, i.e. a region constituted by 3×3 cells, and that constitutes the detection window of the methodology (nine red cells in Figure 1b) (Dalal and Triggs, 2005). This block window is moved along the whole grid with a cell-sized step in order to analyse the complete image; adjacent blocks in a row will thus only differ by a cell column (Figure 1c).

We considered features based on the image gradient (a vector with the directional variation of the intensity) computed at each pixel (Figure 1d), whose vector is characterized by the magnitude and phase (direction), since they are adequate to describe the directional and periodic characteristics of the dunes. In particular, we computed the phase and amplitude histograms, intending to capture the typical edge structure of the local shape of a dune, with a controlled degree of invariance to local geometric and radiometric factors. To obtain them, it was necessary to compute the phase and magnitude histograms of the gradient in each cell. The 180 features that were computed in our experiments for each image block (constituted by nine cells) result from the following:

- 99 features for the magnitude, resulting from 11 bins per cell (considering four unit intervals between a minimum of zero and a maximum of 40);
- 81 features for the phase, resulting from nine bins per cell (considering an angular interval of 20°).

Figure 2 shows an example of these 180 features for the block of Figure 1c. This block includes cells with 'dune' and 'non-dune' labels and permits visual verification of their distinct behaviours: (i) the histogram of the gradient magnitude in a region without dune (the three cells on the column of the right) is concentrated in one narrow range of low values, which means that there are no pixels with a large gradient value, while in regions with dunes, the histogram is frequented along a much wider range of values (the six cells on the left and centre columns) (Figure 2a); (ii) the histogram of the phase (graphically

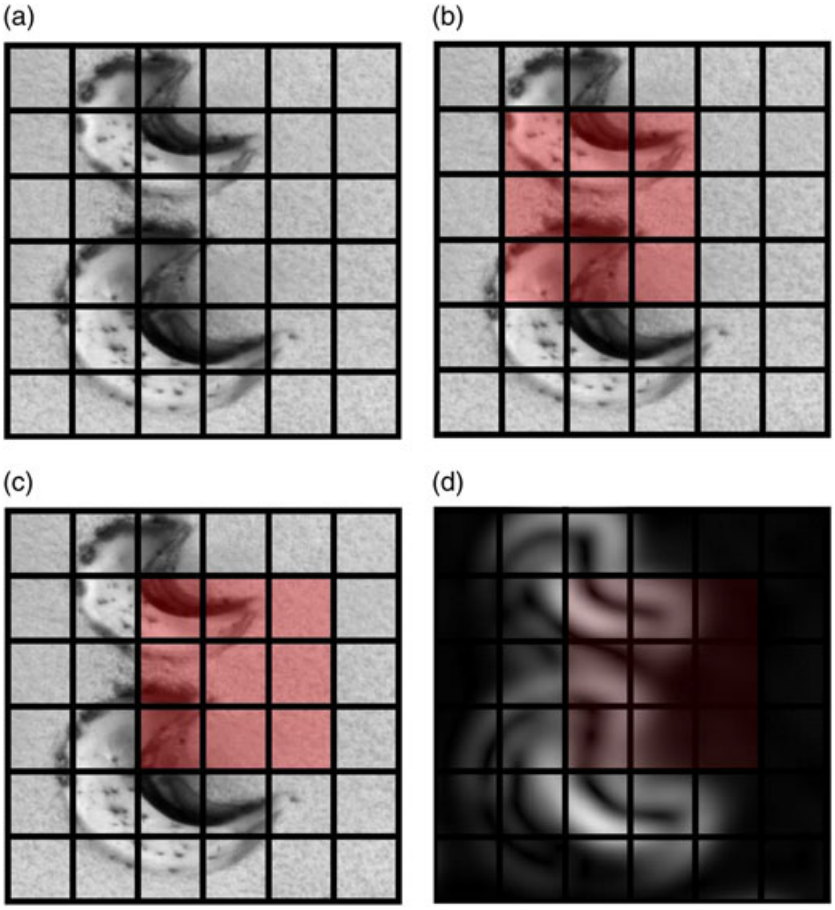

Figure 1. Detail of MOC-NA image E18-00494: (a) tiling an image into cells; (b) constitution of a block (3×3 cells, in red); (c) block advance to the right (one column of cells); (d) gradient magnitude measured in each pixel. (Image credits: NASA/JPL/MSSS.) This figure is available in colour online at wileyonlinelibrary.com/journal/espl

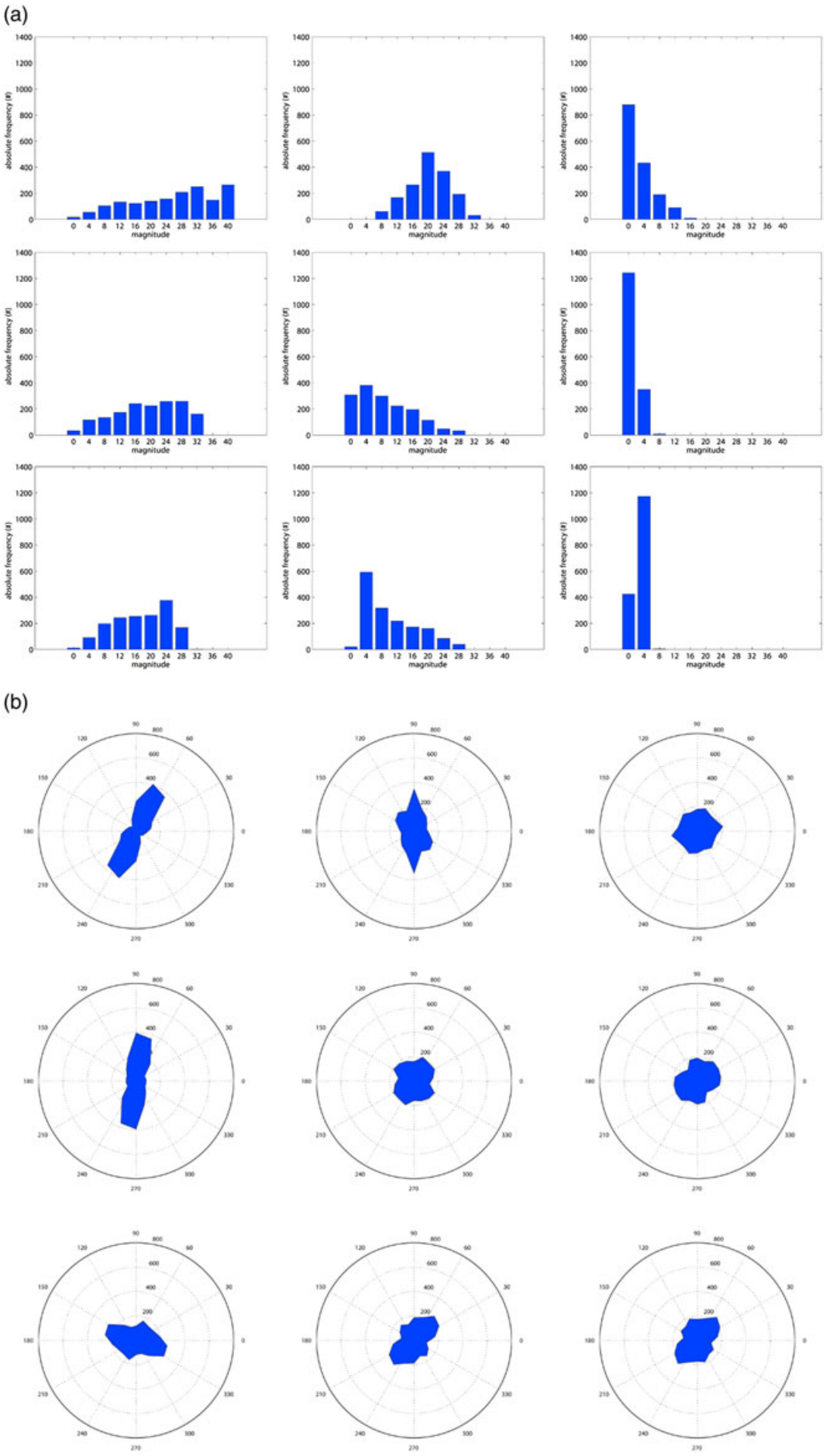

Figure 2. Features extracted for highlighted block in Figure 1c: (a) 11×9 features given by the histograms of the gradient magnitude; (b) 9×9 features given by the directional histograms of the gradient phase. This figure is available in colour online at wileyonlinelibrary.com/journal/espl

represented as a rose of directions) shows the predominant orientation(s) of the texture present in each cell (Figure 2b).

In order to assign a binary label ('dune', 'non-dune') to each cell, it was necessary to evaluate the features extracted in the cell and its eight neighbouring cells (block). Labelling was assigned using supervised learning techniques. In this work two state-of-the-art classifiers were used: (i) SVM-Support Vector Machines (Vapnik, 1995), which is a kernel based approach that transforms data into a higher dimensional space in which it can be separated by a hyperplane; (ii) RF-Random Forests (Breiman, 2001), that models the classification problem using multiple decision trees trained from random subsets of data. These methods were implemented using the free software packages LIBSVM (Chang and Lin, 2011) and RandomForest developed by Leo Breiman and Adele Cutler (www.stat.berkeley.edu/~breiman/RandomForests).

Datasets and Evaluation Strategy

Two datasets of MOC-NA images were used in this paper, representative of most of the surface of the planet and with a good temporal distribution, subject to image availability: one with 160 images containing dunes and another with 70 images of other geomorphological structures that can be confounded with dunes (channels, crater rims, textured terrain, among others). These images have a spatial resolution better than 6·80 m/pixel, going down to 1·45 m/pixel. All images of the first dataset were visually analysed in order to construct a ground-truth for each of them, by manually drawing the contours of the dunes on-screen, which naturally introduced some edge smoothing. One example can be seen in Figure 3: the original grey-scale image is in Figure 3a, the correspondent ground-truth in Figure 3b.

In order to compare the ground-truth with the result produced by the automated classifier, both had to be in the same format. Thus, we had to tile the ground-truth in the same fashion as the original image (Figure 3c). In this image we find three types of cells: 'non-dune' (in yellow), 'dune' (in green) and unclassifiable (in grey). To assign one of these labels to a cell, we computed the area of the block from which it is the centre that is occupied by ground-truth dune: if this area was less than 10% of the number of pixels of the block, the cell was considered 'non-dune'; if it was higher than 30%, the cell was 'dune'; if the area was between 10 and 30%, we considered that any decision would be ambiguous, so we decided not to classify it.

The classifiers (SVM and RF) were trained using images from both datasets (230 images). Since the amount of data is limited we used a five-fold cross-validation method. The total number of images was divided into five subsets (folds), each one containing approximately the same number of dune-cells (for details, see Table I). Four folds are used for training, and the remaining one is used for testing. In this way the images used for training are not present in the test set. This procedure was repeated five times

Table I. Fold distribution.

	Number of images	Number of 'dune' cells	Number of 'non-dune' cells
Total	230	112,029	257,990
Fold 1	46	22,333	49,665
Fold 2	46	22,355	47,476
Fold 3	46	22,387	56,618
Fold 4	46	22,486	51,391
Fold 5	46	22,468	52,840

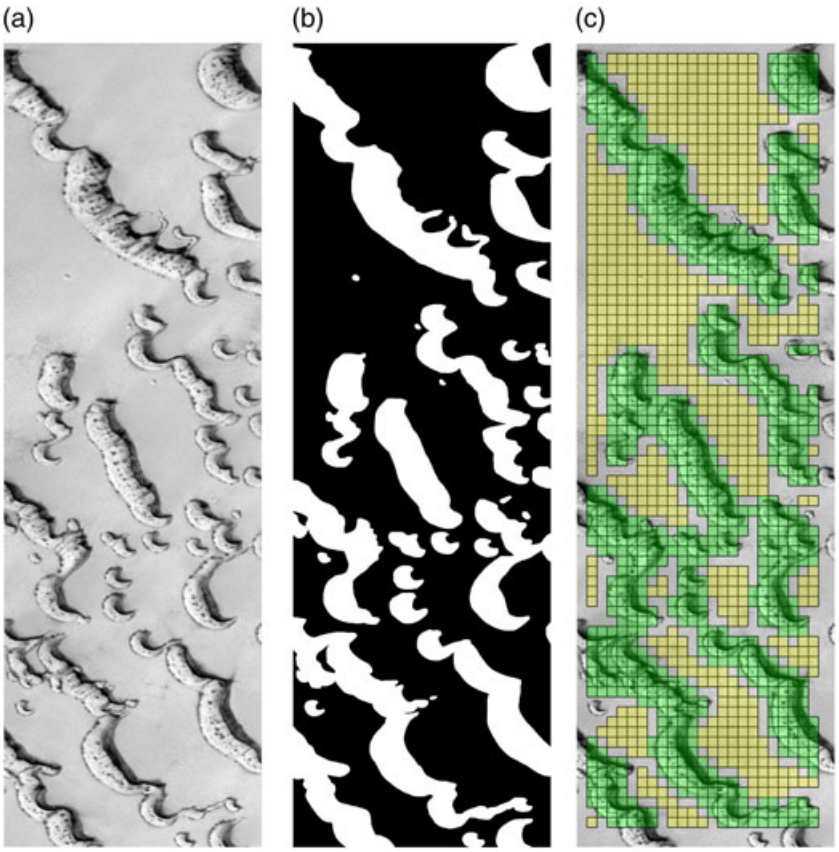

Figure 3. Preparation of the evaluation: (a) original image (MOC-NA E18-00494); (b) manually drawn binary ground-truth; (c) tiling of the ground-truth in cells (green: 'dune'; yellow: 'non-dune'; grey: not subject to classification). (Image credits: NASA/JPL/MSSS.) This figure is available in colour online at wileyonlinelibrary.com/journal/espl

by rotating the folds for training and testing, and a new classifier was trained from scratch each time. Separate statistics were computed for each dataset (with and without dunes) in order to better understand the behaviour of this method in both cases.

The images constituting the first dataset (160 images) include examples of the major types of Martian dunes, identified in Hayward *et al.* (2007): barchan (BC), barchanoid (BN), transverse (TV), dome (DO), linear (LN), star (ST), sand sheet (SS) and other (OT) (Figure 4). Their representation in the dataset reflects to a certain extent their occurrence on the surface of the planet which is dominated by barchans and barchanoid fields; the percentual representation of each type can be seen in Figure 5. Note that some images contain areas with two or more types of dunes.

During the construction of the ground-truth segmentation, we perceived that there are common geometric characteristics between certain types of dunes. This led us to consider another classification analysis scheme, grouping the binary objects into four types of bulk shapes (Figure 6): isolated (mainly barchans and domes); elongated (mainly barchanoids, linear and transverse); compact (sand sheets, and dense combinations of other types) and compact with holes (star and others). This alternative classification yielded a more equivalent distribution (Figure 7) and attenuated the ambiguity of distinguishing

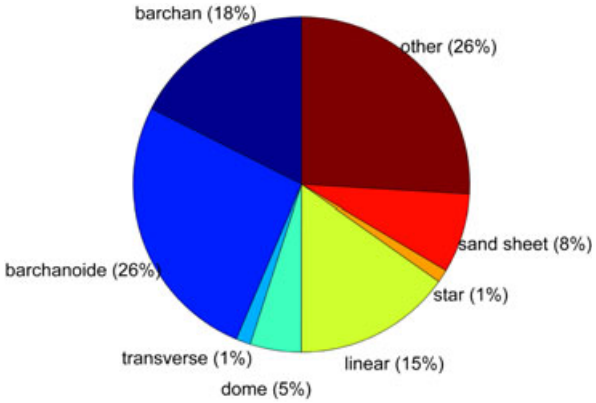

Figure 5. Percentual distribution of the types of dunes in the dataset of 160 images. This figure is available in colour online at wileyonlinelibrary.com/journal/espl

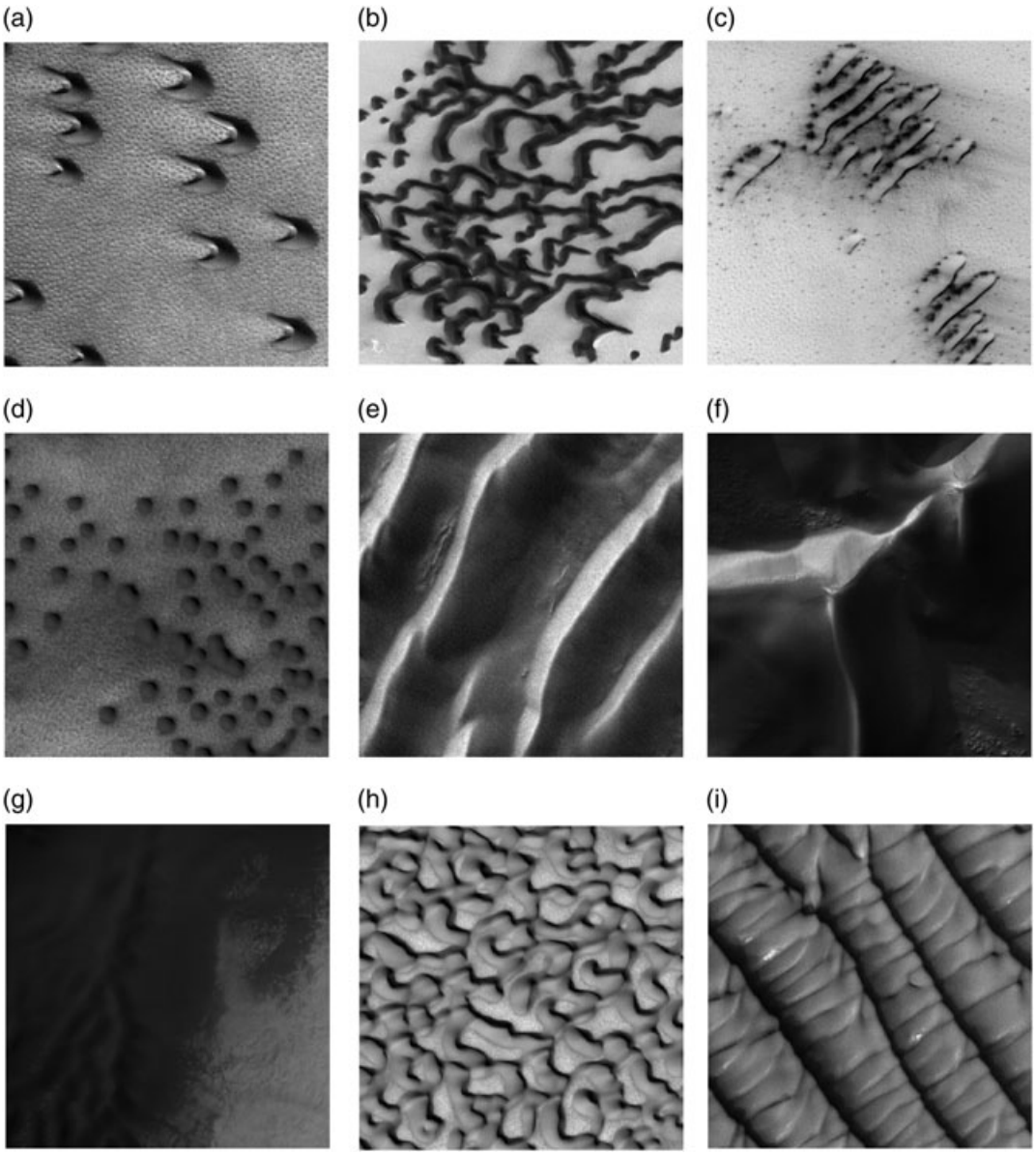

Figure 4. Examples of main Martian dune types from our dataset (the side of each square image is 2500 m): (a) barchan; (b) barchanoid; (c) transverse; (d) dome; (e) linear; (f) star; (g) sand sheet; (h) and (i) other. (Image credits: NASA/JPL/MSSS.)

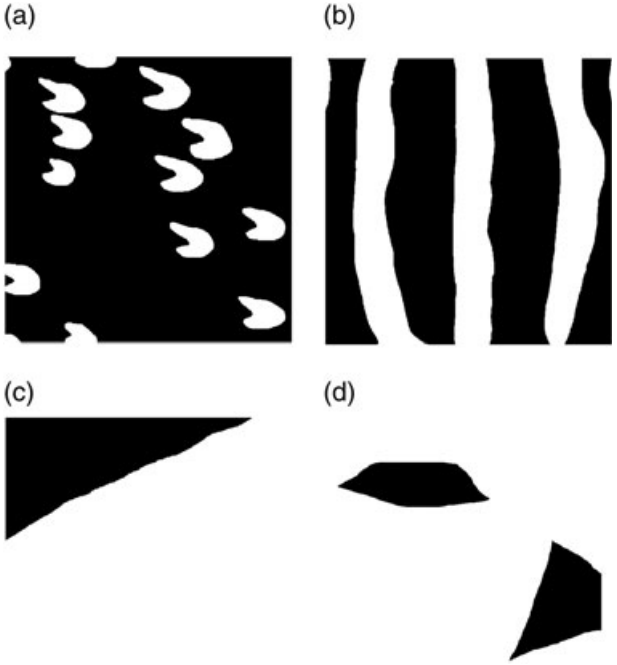

Figure 6. Examples of the four bulk shapes encountered in the binary ground-truth (the side of each square image is 2500 m): (a) isolated; (b) elongated; (c) compact; (d) compact with holes.

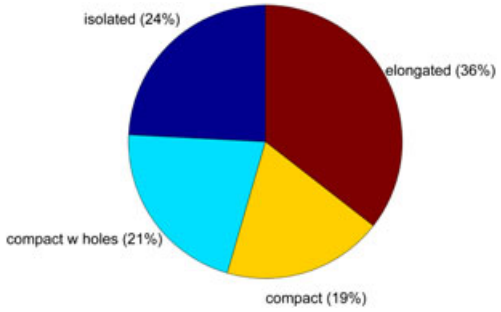

Figure 7. Percentual distribution of the four types of bulk shapes in the ground-truth. This figure is available in colour online at wileyonlinelibrary.com/journal/espl

between, for instance, linear and transverse dunes, especially when an image did not cover a whole dune field.

The performance of the classifier was evaluated through the computation of the following probabilities:

(1) false negatives: $p_{FN} = FN/(FN + TP)$;
(2) false positives: $p_{FP} = FP/(FP + TN)$;
(3) global errors: $p_{error} = p_N \times p_{FP} + p_P \times p_{FN}$.

Here, FN stands for the number of false negative cells ('dune' classified as 'non-dune'), TN is the number of true negative cells ('non-dune' correctly classified), FP is the number of false positive cells ('non-dune' classified as 'dune'), TP is the number of true positive cells ('dune' correctly classified), p_N is the probability of occurrence of negative cells, and p_P is the probability of occurrence of positive cells. Although the features are based on a block of 3×3 cells the output of the classifier is assigned to a single cell (central cell of the block).

Results and Discussion

The proposed method was evaluated with two datasets: the first containing Martian dunes and the second other kinds of geomorphological structures. Ideally we would like the algorithm to segment all dune regions in the first set of images and make no detections in the second.

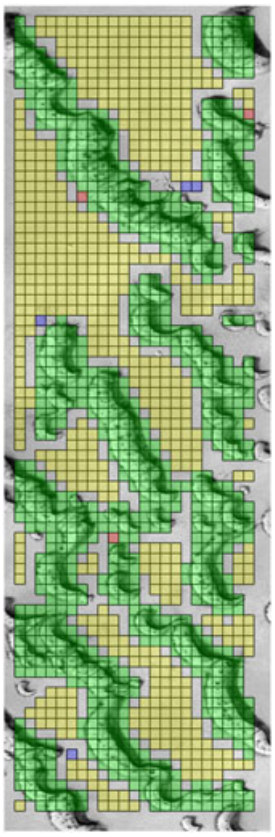

Figure 8. Cell classification for tiled image E18-00494, with SVM (green: TP; yellow: TN; red: FN; blue: FP). This figure is available in colour online at wileyonlinelibrary.com/journal/espl

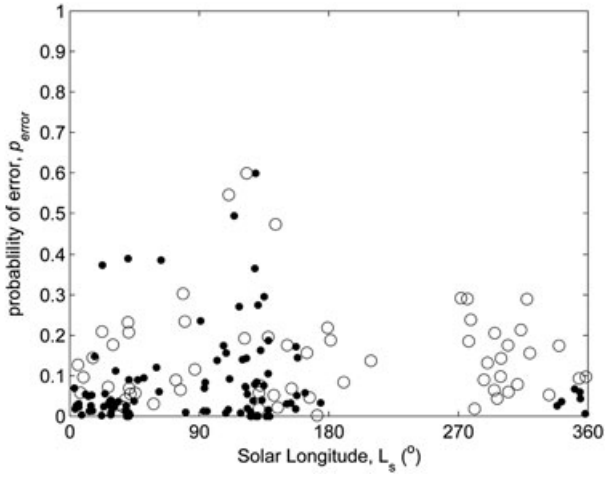

Figure 9. Probability of error as a function of the solar longitude L_s of Mars at the time of image acquisition (open circles: southern hemisphere image; full circles: northern hemisphere image).

Table II. Performance of the classifiers in images with dunes.

	p_{FN}	p_{FP}	p_{error}
SVM	0·085	0·131	0·112
RF	0·080	0·133	0·112

Table III. Performance of the SVM classifier by type of dune.

	Number of images	Number of 'dune' cells	Number of 'non-dune' cells	p_{FN}	p_{FP}	p_{error}
Barchan	31	15,111	33,588	0·077	0·097	0·091
Barchanoid	43	24,889	47,624	0·074	0·064	0·067
Transverse	4	691	3179	0·157	0·059	0·076
Dome	12	5434	8212	0·008	0·374	0·255
Linear	18	22,746	19,455	0·036	0·333	0·175
Star	2	2167	1290	0·164	0·182	0·172
Sand sheet	11	7346	13,819	0·182	0·098	0·127
Other	39	33,645	38,328	0·100	0·116	0·108

Evaluation in the dataset of Martian dunes

In Figure 8 we present the classification results for one of the 160 images in the first dataset (see legend for full explanation of colours). This is evidently a very good result: the vast majority of the cells in the image are well classified, either as 'dune' (833 cells) or 'non-dune' (603 cells), and there are only four false-positive and three false-negative cases, giving a probability of error of only 0·005. It illustrates the kind of result we intend to achieve on a regular basis for any image analysed. It is of course impractical to present the detailed results for the whole 160 images that constitute this dataset. Not all of them show results as good as this particular image, but a vast majority of images present low probabilities of error, as can be seen on Figure 9; for instance, there are 95 images with a probability of error below 0·10 and 137 images below 0·25. There are only six images with a probability of error that is too high for our expectations (above 0·40), where the classifier committed many misclassifications. This is mainly due to the scale issue and was already debated in Bandeira *et al*. (2011).

The results we have obtained for the whole set of images confirm that it is a valid contribution to the automated mapping of dune fields on remotely sensed images. There were 277,524 cells to be classified in the 160 images, and the average global probability of error is about 0·11 (Table II). The probability of false positives is 0·13 and the probability of false negatives is below 0·09. This means that within these 160 images of dune fields, the proposed approach (with either classifier) is capable of correctly classifying a dune cell with a probability of 89%. Since both classifiers achieved very similar performances, in this paper we present a detailed analysis (by dune type and bulk shapes) with only the SVM classifier.

Some care was exercised to include in the set of images examples of most of the Martian dune types normally considered in the literature (Hayward *et al*., 2007). This was done to try and evaluate the response of the methodology to the differing characteristics in shape, dimension and contiguity that

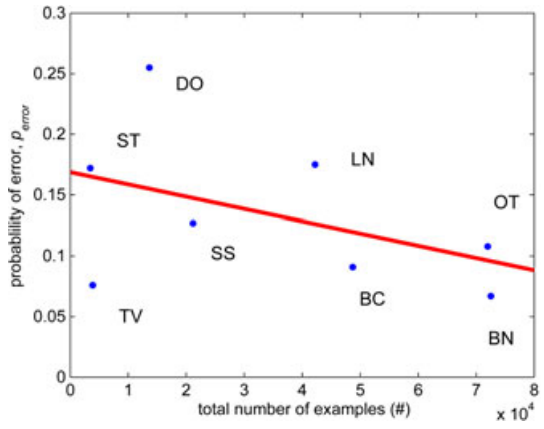

Figure 10. Probability of error as a function of the number of cells present in the images containing a given type of dune [barchan (BC), barchanoid (BN), transverse (TV), dome (DO), linear (LN), star (ST), sand sheet (SS) and other (OT)]. This figure is available in colour online at wileyonlinelibrary.com/journal/espl

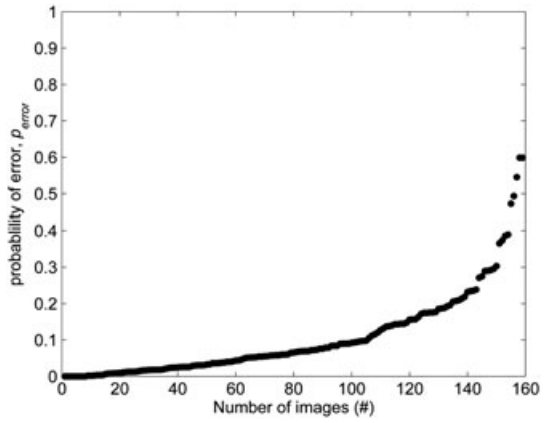

Figure 11. Sorted probability of error for the 160 images of the dataset.

Table V. Performance of the classifiers in images with non-dune structures.

	p_{FN}	p_{FP}	p_{error}
SVM	—	0·081	0·081
RF	—	0·082	0·082

Table IV. Performance of the SVM classifier by bulk shape of ground-truth.

	Number of images	Number of 'dune' cells	Number of 'non-dune' cells	p_{FN}	p_{FP}	p_{error}
Isolated	50	16,415	50,715	0·059	0·149	0·128
Elongated	53	42,137	56,495	0·065	0·148	0·112
Compact	29	26,393	26,228	0·094	0·134	0·114
Compact with holes	28	27,084	32,057	0·113	0·080	0·095

the dunes present. The results obtained with the SVM classifier, considering the distribution of the dune types in the 160 images, can be appreciated in Table III. The range of values again highlights the robustness of the methodology. Barchan and barchanoid types achieved the best performance with a probability of error below 0·09; however, the star dunes, though poorly represented, produced the worst probability of error, but this was only close to 0·21. Figure 10 illustrates this clear trend of the decrease of the probability of error as a function of the number of cells present in the images containing a given type of dune. The more a given type is represented the lower the probability of error is.

As explained earlier, we also evaluated the classification results obtained with the SVM classifier according to the four categories that resulted from an analysis of the ground-truth shapes; this can be seen in Table IV. Once again the results were very good and similar between the four types. The best result was about 0·10 for the compact with holes and the worst

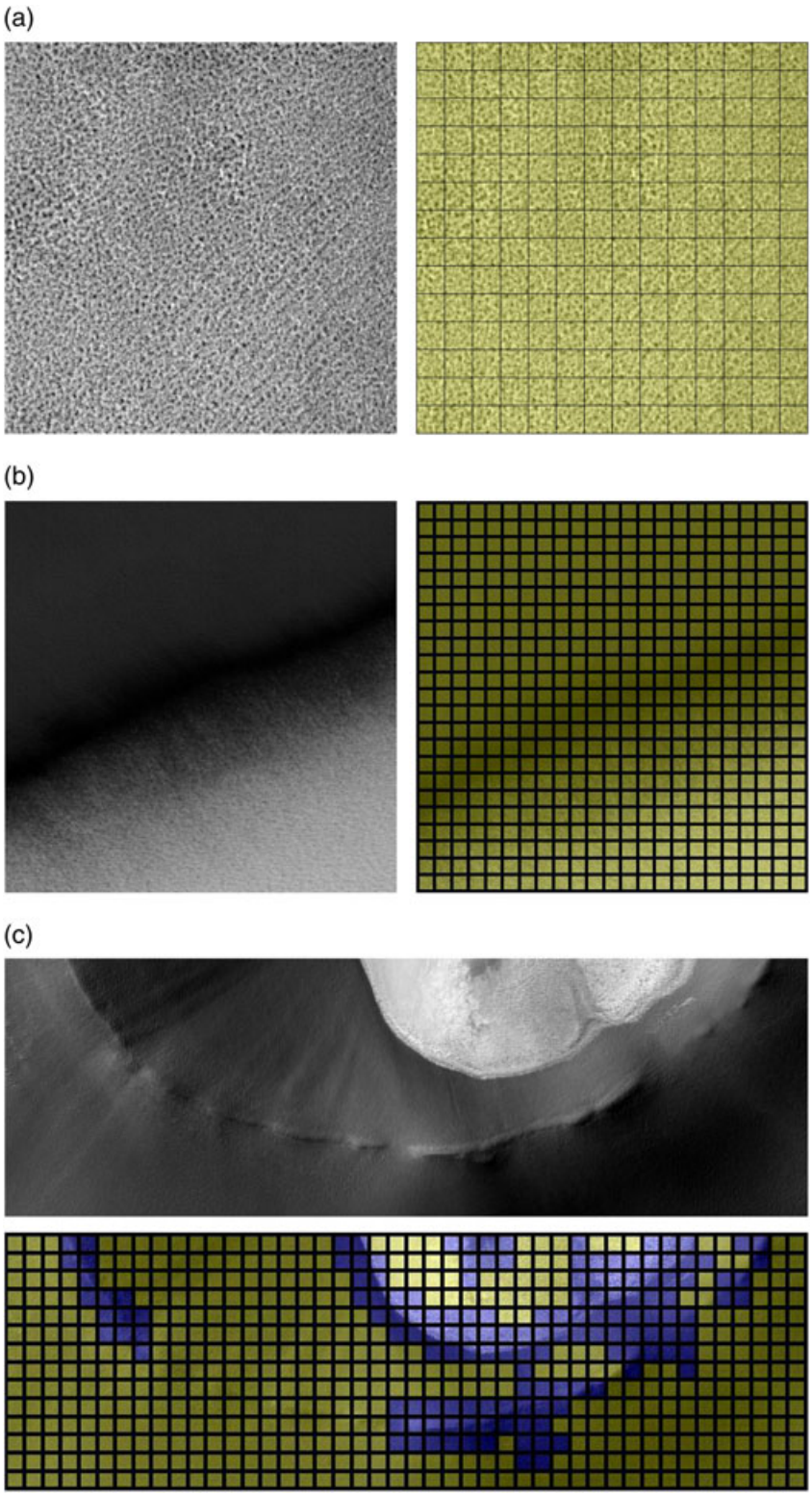

Figure 12. Classification of images with non-dune structures: (a) positive example (detail of FHA-00471; (b) positive example (detail of M00-00133); (c) negative example (detail of E01-01028) (yellow: TN; blue: FP). This figure is available in colour online at wileyonlinelibrary.com/journal/espl

was 0·12 for the elongated type, which were very close to the average result obtained for the global set of 160 images as a whole.

In Figure 11 we show the distribution of the probability of error according to the solar longitude of Mars at the moment when the respective image was acquired. This shows that this factor does not influence the results, and the same is true for other factors that could affect the conditions of image acquisition or the local conditions on the surface of the planet.

Evaluation in the dataset with other Martian structures

In the previous subsection the algorithm was evaluated assuming that the images contain dune fields to be segmented. This subsection considers the performance of the algorithm when the test images do not contain dunes, but other geomorphological structures instead. The classifier was trained as before, using dune and non-dune images in a five-fold cross-validation framework. However, only the non-dune images in the test set were used in the computation of the statistics. Table V shows the classification results for both classifiers. As it can be seen, the probability of false positives is about 0·08. This means that approximately 8% of negative cells are wrongly classified as dunes. Figures 12a and 12b shows positive examples and Figure 12c negative examples. The method manages to correctly classify a textured non-dune region and a smooth transition in Figures 12a and 12b but fails in the presence of a crater rim, Figure 12c, which is wrongly classified as dune. This error can be explained by the fact that the crater rim is locally similar to a dune crest.

Conclusion/Future Work

The continuous flow of high resolution images means that there is no lack of data to be analysed; however that analysis is mostly conducted by human operators and thus eminently subjective. That was one of the main motivations for our work in the development of an automated method for the identification of dunes/dune fields.

The main conclusion is that the performance of our methodology based on gradient histograms combined with a supervised learning scheme (SVM or RF) can be considered very good independently of the way in which the datasets are analysed: whole, by type of dune, bulk shape, exclusively with dune images or including other geomorphological structures, the average probability of error is about 0·11. In 160 images only a handful presents an error that can be considered high. Those images will be scrutinized in detail in order to understand where the classifier went wrong and improve its performance; ideas for future work include the extraction of other types of features and the use of a multi-scale strategy.

We consider that doubling the number of images analysed and introducing six types of Martian dunes not studied before (Bandeira *et al.*, 2011), with an overall performance of about 90% of correct detections is a considerable advance, even if the global average error increased slightly in comparison to our previous work. The huge amount of data analysed (hundreds of thousands of cells, corresponding to almost half a billion pixels) with such high detection rate shows that the method is statistically robust for automated dune detection.

Given the efficiency of the methodology we aim to take our research one step further and collect quantitative parameters that can lead to an objective characterization of the dunes identified.

References

Bandeira L, Marques JS, Saraiva J, Pina P. 2010. Automated detection of sand dunes on Mars. In *Image Analysis and Recognition*, Campilho A, Kamel M (eds), Lecture Notes in Computer Science vol. 6112. Springer: Berlin-Heidelberg; 306–315.

Bandeira L, Marques JS, Saraiva J, Pina P. 2011. Automated detection of Martian dune fields. *IEEE Geoscience and Remote Sensing Letters* **8**(4): 626–630.

Bishop MA. 2010. Nearest neighbor analysis of mega-barchanoid dunes, Ar Rub' al Khali, sand sea: the application of geographical indices to the understanding of dune field self-organization, maturity and environmental change. *Geomorphology* **120**: 186–194.

Bourke MC, Balme M, Beyer R, Williams K, Zimbelman J. 2006. A comparison of methods used to estimate the height of sand dunes on Mars. *Geomorphology* **81**(3/4): 440–452.

Bourke MC, Lancaster N, Fenton LK, Parteli EJR, Zimbelman JR, Radebaugh J. 2010. Extraterrestrial dunes: an introduction to the special issue on planetary dune systems. *Geomorphology* **121**(1/2): 1–14.

Breiman L. 2001. Random Forests. *Machine Learning* **45**(1): 5–32.

Chang C-C, Lin C-J. 2011. LIBSVM: a library for support vector machines. *ACM Transactions on Intelligent Systems and Technology* **2**(3): article 27. Software available at http://www.csie.ntu.edu.tw/~cjlin/libsvm

Chowdhury PR, Deshmukh B, Goswami AK, Prasad SS. 2011. Neural network based dunal landform mapping from multispectral images using texture features. *IEEE Journal of Selected Topics in Applied Earth Observations and Remote Sensing* **4**(1): 171–184.

Dalal N, Triggs B. 2005. Histograms of oriented gradients for human detection. In *Proceedings of CVPR2005, vol. 1*. IEEE Press: New York; 886–893.

Ewing RC, Kocurek G, Lake LW. 2006. Pattern analysis of dune-field parameters. *Earth Surface Processes and Landforms* **31**: 1176–1191.

Fenton LK, Hayward RK. 2010. Southern high latitude dune fields on Mars: morphology, aeolian inactivity, and climate change. *Geomorphology* **121**: 98–121.

Hayward R, Mullins K, Fenton LK, Hare T, Titus T, Bourke MC, Colaprete A, Christensen P. 2007. Mars global digital dune database and initial science results. *Journal of Geophysical Research – Planets* **112**(E11): E1107.

Hugenholtz CH, Barchyn TE. 2010. Spatial analysis of sand dunes with a new global topographic dataset: new approaches and opportunities. *Earth Surface Processes and Landforms* **35**: 986–992.

McKee ED. 1979. Introduction to a study of global sand seas. In *A Study of Global Sand Seas*, McKee ED (ed.). University Press Pacific: Honolulu, HI: 1–19.

Silvestro S, Fenton LK, Vaz DA, Bridges NT, Ori GG. 2010. Ripple migration and dune activity on Mars: evidence for dynamic wind processes. *Geophysical Research Letters* **37**: L20203.

Vapnik VN. 1995. *The Nature of Statistical Learning Theory*. Springer-Verlag: Berlin.